



Enhanced photoelectrocatalytic reduction dechlorinations of PCP by Ru-Pd BQDs anchored Titania NAEs composites with double Schottky junctions: First-principles evidence and experimental verifications

Shiying Fan^a, Xinyong Li^{a,b,*}, Jing Tan^a, Libin Zeng^a, Zhifan Yin^a, Moses O. Tadé^b, Shaomin Liu^b

^a State Key Laboratory of Fine Chemicals, Key Laboratory of Industrial Ecology and Environmental Engineering (MOE), School of Environmental Science and Technology, Dalian University of Technology, Dalian 116024, China

^b Department of Chemical Engineering, Curtin University of Technology, Perth, WA 6845, Australia

ARTICLE INFO

Keywords:

Photoelectrocatalytic reductive dechlorinations
Polychlorinated compounds
Ru-Pd bimetallic quantum dots
Titania nanotube arrays
Double Schottky junctions

ABSTRACT

Novel palladium (Pd) and ruthenium (Ru) Bimetal Quantum Dots (BQDs) co-anchored on Titania nanotube arrays electrodes (NAEs) bearing double Schottky junctions with superior photoelectrochemical conversions and photoelectrocatalytic reductive dechlorination (PECRD) properties were successfully developed and constructed by facial two-step electrochemical strategy. The PECRD of toxic Pentachlorophenol and photoelectrochemical conversions over the afore-designed bimetallic Pd and Ru BQDs co-anchored TiO₂ (101) nanotube array electrodes (Ru-Pd BQDs/TiO₂ NAEs) composites have been systematically investigated both theoretically and practically. A remarkable enhancement of photoelectrochemical conversion efficiency of 14.10% as compared to that of the pure TiO₂ NAEs (0.45%) in the Ru-Pd BQDs/TiO₂ NAEs composites has been successfully achieved, and pentachlorophenol (PCP) species could be PECRD over 90% under the optimum conditions. Various physico-chemical techniques including UV–vis spectroscopy, XRD, SEM/TEM/EDX, PL, EIS, SPV and XPS were employed to systematically characterize the crystal-, electronic and micro-interfacial structures of the composites with double Schottky junction, respectively. All of the studies implied that the marvelous enhancement of separation efficiency of photo-generated electron–hole pairs is mainly caused by the Schottky-barriers as derived from the interfacial interaction within the Ru-Pd BQDs/TiO₂ NAEs metal-semiconductor composites. The Ru-Pd BQDs/TiO₂ NAEs bearing double Schottky-junctions would greatly facilitate the interfacial charge transfer followed by fully utilization of the photo-generated electrons for PECRD of PCP species. The DFT calculations clearly indicated that the number of impurity (i.e., co-anchored Ru-Pd BQDs) energy levels near Fermi surface increased, promoting electron energy transition and reduces the band gap, which suggesting a better reduction capability. Overall, this work shall provide brand new insight for molecular design of Bimetal Quantum Dots (BQDs) assembled onto Titania NAEs composites with superior performance for both environmental eliminations and green energy conversions and could significantly deepen our understanding to the catalytic dechlorination pathways of typical environmental toxic polychlorinated compounds over multifunctional nanocatalytic materials.

1. Introduction

Polychlorinated compounds is an important organic chemical with widespread application in agriculture and industry [1]. It is highly toxic and persistent in the environment and can accumulate in living organisms resulting in negative effects including carcinogenicity and acute toxicity [2]. Investigation on polychlorinated compounds degradation has attracted increasingly more attention of all over the world. A solution to the problem of managing excessive amounts of

polychlorinated compounds in the wastewater is the adoption of sustainable energy sources created using green chemistry. Among them, Photocatalytic redox technology using functional materials has been proved to be an effective strategy for elimination of polychlorinated compounds from environment [3–5]. Especially, photo-generated electrons in the photocatalytic reduction reaction of semiconductor mediated photo-induced interfacial redox process could completely eliminate containments without forming more toxic organic compounds, which can be usually formed in the photocatalytic oxidation

* Corresponding author at: State Key Laboratory of Fine Chemicals, Key Laboratory of Industrial Ecology and Environmental Engineering (MOE), School of Environmental Science and Technology, Dalian University of Technology, Dalian 116024, China.

E-mail address: xyli@dlut.edu.cn (X. Li).

<https://doi.org/10.1016/j.apcatb.2018.01.043>

Received 19 September 2017; Received in revised form 29 December 2017; Accepted 18 January 2018

Available online 31 January 2018

0926-3373/ © 2018 Elsevier B.V. All rights reserved.

reactions [6–8]. Whereas, the efficiency of photocatalytic reduction for polychlorinated compounds is still low in terms of future technological applications. Hence, further enhancing the reaction efficiency and deeply investigating the reaction mechanism of photocatalytic reduction are key scientific issues.

Up to now, tremendous efforts have been devoted to rational design efficient solar-light harvesting nanostructured materials with speedy interfacial charge transfer, marvelous high activity, stability and recyclability [9,10]. It is well known that TiO_2 has been proved as a promising photocatalyst because of its high photosensitivity, non-toxicity, strong oxidizing power and long-term stability [11]. Despite intense research works, many scientific problems remained to be solved and/or explored. Bunch of shortcomings including the failure to control charges recombination, fewer active sites on the surface of TiO_2 and the lack of visible light utilization have significantly confined its potential application [12]. Numerous previous studies indicated that noble metals surface derivations including grafting and/or anchoring etc., such as Pt, Au, Pd, Rh, Ni, Cu, Ag etc. could build an interfacial electric field, band bending and forming a Schottky type contact and/or junctions with n-type TiO_2 which would facilitate interfacial transfer of photo-generated electrons from the conduction band (CB) of TiO_2 to the noble metals, and thus enhancing the optical, electrochemical (EC) and photoelectrochemical (PEC) properties of metal-semiconductor composites [13–15]. Meanwhile, the afore-mentioned surface derivations mainly plays two synergetic roles in steering the charge kinetics in photocatalysis: i) trapping charge carriers to promote electron-hole separation by forming an interface including Schottky barrier with the semiconductor; and ii) serving as a highly active reaction site to supply the trapped charges for redox reactions over the surface-interface of the composites, and finally contribute to the marvelous enhancement of catalytic activity and selectivity [16].

Recently, the bimetallic nanostructures have attracted significant attention due to their unique optical, electronic, magnetic and catalytic properties. The development of highly dispersed bimetallic nanomaterials including Nanoparticles (NPs), Nanotubes (NTs), Nanocages and Quantum Dots (QDs) etc., provides an opportunity to molecular design catalytically-active advanced functional materials [17–20]. The enhanced performance of bimetallic nanoparticles can be rationalized by electronic (charge transfer), geometric and synergistic effects [21,22].

Ruthenium (Ru) [23] and Palladium (Pd) [24] NPs catalytic materials have shown marvelous activity in catalysis including photocatalytic hydrodechlorination (HDC) due to their physico-chemical characteristics including specific ability and capability for tremendously facilitating the hydrogenolysis of C–Cl bonds over the interface of Ru and Pd co-catalysts. Moreover, it is commonly known that the hydrogen over-voltage (HOV) of palladium (Pd) based electrodes is slightly higher than that of Pt and much lower than those of Ag and Cu, which imply that the electrochemical feature of Pd bearing slightly higher HOV can moderately suppress hydrogen formation. In 2014, Dr. Cody's team reported that highly dispersed Ru NPs/ TiO_2 catalytic materials shows superior selectivity and activity toward direct deoxygenation [25,26]. Carlos's systematically works revealed the surface deposition of Ru onto TiO_2 NPs would finally lead to the forming of highly efficient catalytic materials for hydrogenation of xylose [27]. Prakash reported that photocatalytic hydrodechlorination of 4-chlorophenol in an aqueous phase over a 4% Ru–1% Pd/ TiO_2 NPs catalyst were carried out in a three-phase slurry reactor, and they claimed that the reaction rate of HDC over Ru-Pd bimetallic catalysts was much higher than that of Ru monophasic catalyst [28]. Baeza's work clearly indicated that a significant higher activity improvement of 4-chlorophenol HDC over bimetallic Pd-Rh NPs has been accomplished compared with that of monometallic Pd and Rh NPs under equivalent conditions [29]. Notably, it has been learnt from previously reports that bimetal surface derivations including co-doping plays an important role in improving the photocatalysis of titania dioxide, whereas, the more detail information for structure of the metal–support interface and the

growth mechanism of the supported metal atoms at electronic and atom level still remains unclear. In fact, to deeply uncover the metal–support interaction is essential for detail understanding the mechanism of photoelectrocatalytic reductive dechlorinations (PECRD) of PCCs. Regarding of this issue, computational approaches are thought to be one of the most powerful means to explore the metal–support interaction at the atomic and electronic level [30]. For instance, DFT has been widely implemented for elucidating the atom and electron transfer between metal particles and oxide supports, detailed structure of interface, and the mechanism of catalytic hydrogenation and oxidations [31–36].

Herein, taking into the concerns and considerations of designing efficient light harvesting nanomaterials with marvelous activity, stability and recyclability towards highly efficient environmental eliminations and green energy conversions in terms the point view of future practical applications, we have now successfully designed and prepared novel Ru-Pd Bimetallic Quantum Dots (BQDs) with confined electronic structures and specific micro-structures followed by assembling (anchoring, or grafting) them onto the inner and outer of titanium nanotubes arrays electrodes (NAEs), i.e., Ru-Pd BQDs/ TiO_2 NAEs bearing dual Schottky-junctions with superior properties including photoelectrochemical and photoelectrocatalytic performance. Furthermore, for getting a deep insight into the outstanding physicochemical characteristics of the double Schottky-junctions, various on-line and/or off-line physical techniques including EIS, SPV and XPS have now been intensively used to elucidate and investigate the photo-induced redox behavior and the kinetics of interfacial charge transfers as well as the dechlorination mechanism over the composites. Finally, Density Functional Theory (DFT) has been adopted to further study the crystal and electronic structures as well as gap energetics of the composites at the atomic and electronic state level. This work will provide a brand new strategy for molecular design of functional composites composed of BQDs and NTs bearing Schottky-junctions with marvelous properties in both environmental elimination and green energy fields. In addition, this research will further strengthen a deeper insight for detail mechanism of PECRD of PCCs, which is of environmental significance.

2. Experimental

2.1. Preparation of Ru-Pd BQDs/ TiO_2 NAEs

TiO_2 NAEs were fabricated by the anodic oxidation method. Prior to anodization, the titania foil was first mechanically polished with different abrasive papers (240#, 400#, 600#, 800#, 1000#, 1200#) and ultrasonically cleaned with alcohol and cold distilled water for 15 min, respectively. Then they were chemically etched by immersing them in a mixture of HF and HNO_3 acids ($\text{HF}:\text{HNO}_3:\text{H}_2\text{O} = 1:4:5$ in volume) for 30 s, followed by rinsing with deionized water. Electrochemical experiments were carried out at room temperature using a DC power source. The pretreated Ti foil served as the working electrode and Pt foil as the counter electrode. The anodizing voltage varied from 0 to 20 V with an increasing rate of 100 mV s^{-1} and was kept at 20 V for 30 min. The electrolyte was 0.2 wt% HF in water. After anodic oxidation, the samples were annealed at 500°C in oxygen for 1 h with heating and cooling rates of 2°C min^{-1} to convert the amorphous phase to the crystalline one.

The Ru and Pd BQDs were deposited on the TiO_2 NAEs by facial two-step electrochemical strategy. The as-prepared TiO_2 NAEs were immersed in a 10 mM RuCl_3 solution for 5 min, then moved into 0.1 M NaCl solution to undergo electrodeposition at -2 V for 1 s, achieving a uniformity deposition of Ru QDs within the nanotube internal surface. This procedure was repeated five times to get an optimum amount of Ru QDs. And the Pd QDs loaded on the TiO_2 NAEs internal surface following the same technique.

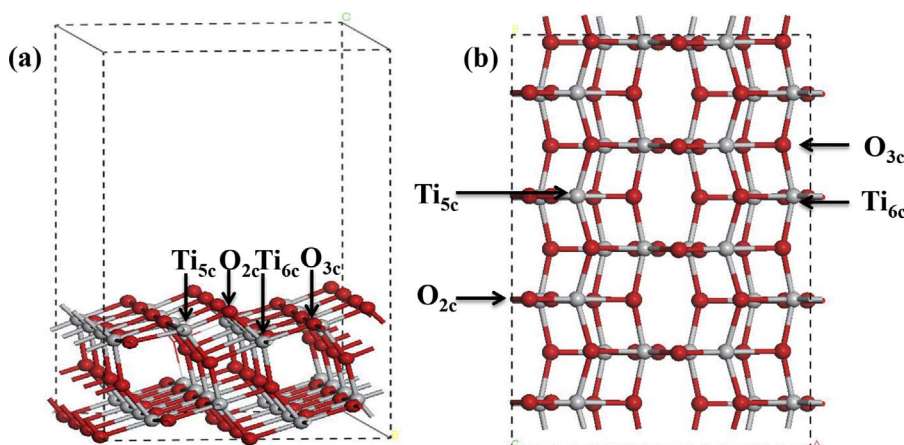


Fig. 1. Side (a) and top (b) views of the anatase TiO_2 (101) surfaces. The red is an O atom and the grey is a Ti atom. (For interpretation of the references to colour in this figure legend, the reader is referred to the web version of this article.)

2.2. Characterization of Ru-Pd BQDs/ TiO_2 NAEs

The morphological of the Ru-Pd BQDs/ TiO_2 NAEs based composites were characterized using scanning electron microscopy (SEM, Hitachi S-4800, Japan Hitachi Company) operating an accelerating voltage of 30 kV and energy dispersive X-ray (EDX, JSM-6360LV). Transmission electron microscopy images were taken on a Tecnai F30 with an acceleration voltage of 300 kV. X-ray diffraction (XRD) patterns were obtained on a Rigaku D/max diffractometer with $\text{Cu K}\alpha$ radiation ($\lambda = 0.15418 \text{ nm}$). X-ray photoelectron spectroscopy (XPS) (PHI 5600 mode) examined the surface properties and composition of the composites. Photoluminescence (PL) spectra were studied using a Hitachi F-4500 excited at ($\lambda = 325 \text{ nm}$) fluorescence spectrophotometer in air. A surface photo voltage (SPV) measurement system used in this investigation consisted of a monochromator (model Omni- λ 3005) and a lock-in amplifier (model SR830-DSP) with an optical chopper (model SR540) running at a frequency of 20 Hz. Transient formation and subsequent decay of photogenerated charges were characterized using a Laser Flash Photolysis spectrometer (LP920, Edinburgh Instruments Ltd., UK). Photoluminescence (PL) spectra of the electrodes were collected using a Hitachi F-4500 (excited at $\lambda = 325 \text{ nm}$) fluorescence spectrophotometer in air at room temperature. Electron spin resonance (ESR) of radicals spin-trapped by spin-trap reagent DMPO were recorded (ECS106 X-Band spectrometer, Bruker, Germany).

2.3. Photoelectrocatalytic reductive dechlorination of pentachlorophenol

Typically, as one member of polychlorinated family compounds, pentachlorophenol (PCP) has been taken as a target for photoelectrocatalytic reductive dechlorinations (PECRD) in this work. The PECRD of PCP toxic moleculars was performed in a home-made quartz glass reactor with a three electrodes cell (shown in Fig. S1), which composed of a Ru-Pd BQDs/ TiO_2 NAEs as working electrode, a RuO_2 film on Ti substrate (RuO_2/Ti) electrode as the counter electrode and a saturated calomel electrode (SCE) served as the reference electrode, respectively. The RuO_2/Ti electrode, which has been fabricated using the Siripala's method [37], was selected as the counter electrode due to its lower over potential of oxygen evolution. A 300W high-pressure mercury lamp with a maximum wavelength of 365 nm was employed as the light source, and an electrochemical workstation (CHI760C) supplied bias potential. Forty milliliters of PCP 2-propanol solution of a given concentration was placed in the reactor. The electrolyte was purged with bubbling Ar gas to get rid of the oxygen in the whole reaction process. The PECRD experiments were carried out at different bias potential, initial solution pH and liquid water content.

2.4. Kinetics of the photoelectrocatalytic reductive dechlorination experiments

The kinetics of PECRD of PCP were adjusted to a Langmuir–Hinshelwood model [38]:

$$\ln(\text{PCP}_0/\text{PCPt}) = kt$$

where k is the kinetic constant given by the slope of the graph of $\ln(\text{PCP}_0/\text{PCPt})$ versus t and PCP_0 is the initial concentration of the organic pollutant.

2.5. Analytical methods

Concentration of PCP was quantified with a Waters 2695 HPLC (Waters China Ltd.) equipped with a C^{18} reversed phase column and an L-2996 UV–vis detector. The mobile phase for PCP consisted of 70% methanol solution (1% acetic acid) and 30% ultrapure water (1% acetic acid). The flow rate was 1 mL min^{-1} and the detector wavelength was 305 nm for PCP and 280 nm for phenol (PhOH). The immediate products were detected by LC–MS (AGILENT 6410, USA) with XDB- C^{18} column ($4.6 \times 50 \text{ mm}$) at a flow rate of 1.0 mL min^{-1} . The mobile phase is CH_3OH (2% CHOOH): H_2O (2% HCOOH) = 0.6: 0.4.

2.6. Computational method and details

In this study, all the quantum calculations of the structures were carried out by CASTEP module in Materials Studio 6.0 software package. The exchange–correlation potential was described by the Perdew–Wang (PW91) exchange–correlation function. Ultrasoft pseudopotentials were used to describe the ionic cores. The wave functions were expanded in a plane wave basis set with a cutoff energy of 380 eV. The generalized gradient approximation (GGA) was chosen here to describe the effects of exchange and correlation. The geometries were optimized using a BFGs method [39–41].

The anatase TiO_2 (101) surface was represented as a $p(2 \times 3)$ slab with a thickness of four O–Ti–O layers ($10.32 \times 15.20 \times 17.89 \text{ \AA}$). The initial crystal structure of anatase TiO_2 was built according to previous experimental work [42]. The neighboring slabs were separated in the direction perpendicular to the surface by a vacuum region of 12 \AA . Top and side views of the anatase TiO_2 (101) surface was shown in Fig. 1.

During the geometric optimization, the two bottom layers were fixed equivalent to bulk structure, while the rest of the atoms were allowed to relax freely. To study the interactions between Ru–Pd and titania surface, adsorption energy is defined as

$$E_{\text{ads}} = E(\text{Pd-Ru BQDs}/\text{TiO}_2) - E(\text{TiO}_2) - E(\text{Pd}) - E(\text{Ru})$$

The binding energy is defined as

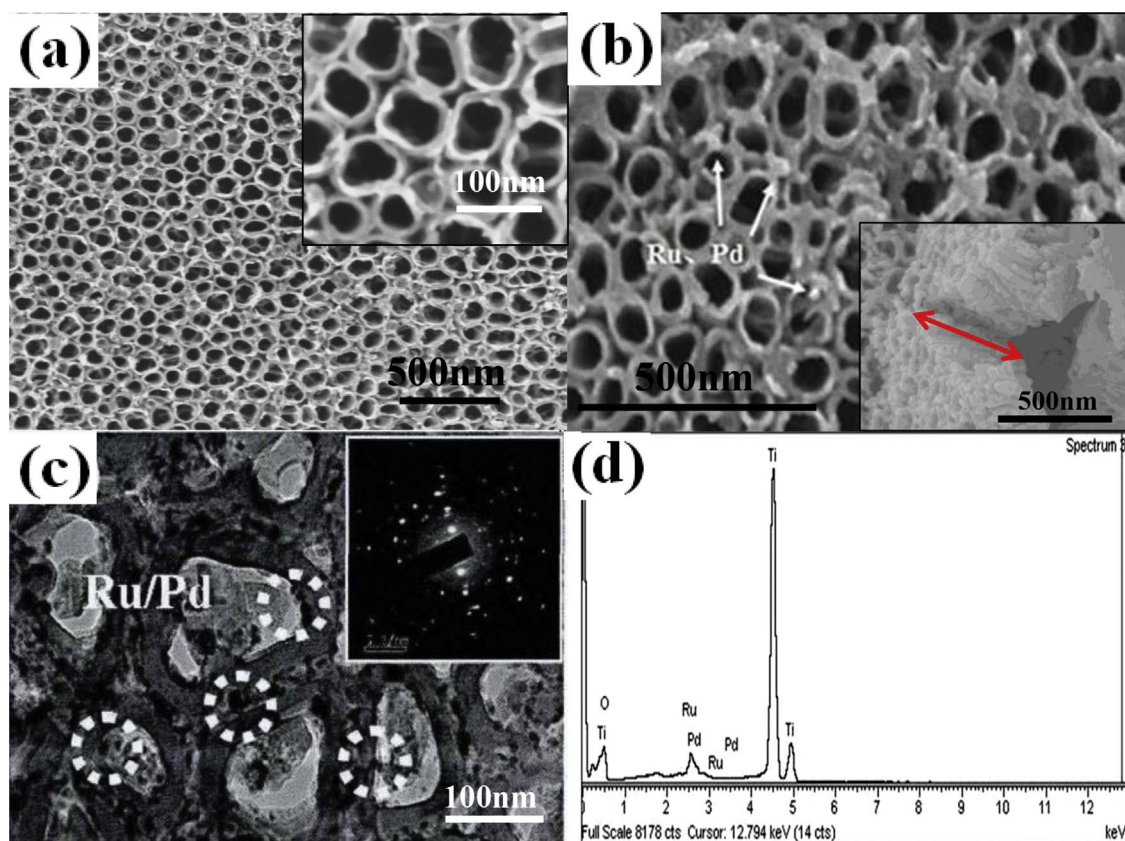


Fig. 2. (a) Top surface SEM view of TiO_2 NAs, the inset shows the images of TiO_2 NAs at high magnification; (b) Top surface SEM view of Ru-Pd BQDs/ TiO_2 NAs, the inset shows the side view of Ru-Pd BQDs/ TiO_2 NAs at high magnification; (c) TEM of as prepared Ru-Pd BQDs/ TiO_2 NAs and the inset shows SAED images; (d) Corresponding EDX pattern of the Ru-Pd BQDs/ TiO_2 NAs.

$$E_{\text{bind}} = [2E(\text{Pd-Ru BQDs}/\text{TiO}_2) - E(\text{Pd}) - E(\text{Ru}) - E(\text{Pd QDs}/\text{TiO}_2) - E(\text{Ru QDs}/\text{TiO}_2)]/2$$

where $E(\text{Pd-Ru BQDs}/\text{TiO}_2)$, $E(\text{TiO}_2)$, $E(\text{Ru})$, $E(\text{Pd})$, $E(\text{Ru QDs}/\text{TiO}_2)$ and $E(\text{Pd QDs}/\text{TiO}_2)$ are the total energies of the TiO_2 substrate with Pd and Ru, the bare TiO_2 substrate, the isolated Ru or Pd adatom in gas phase, the energies of the TiO_2 substrate with Ru or Pd QDs, respectively. E_{bind} gives the adsorption energy of the adsorbed Ru and Pd atoms on the TiO_2 system; Positive values of E_{ads} and E_{bind} correspond to energetically stable adsorption and binding, respectively [43].

The test calculations with different k-point ($2 \times 1 \times 1$) for single Pd and/or Ru adatoms on perfect anatase TiO_2 (101) surface were carried out. The medium-point sampling has been taken in the present study. All these models are calculated under the same calculation conditions to ensure the consistency of whole calculation.

3. Results and discussions

3.1. Characterization of Ru-Pd BQDs/ TiO_2 NAs

The morphologies of the TiO_2 nanotube arrays (NAs) were observed using SEM and TEM. Fig. 2a is a low-magnification SEM image of the as-synthesized TiO_2 NAs, which reveals a regularly arranged pore structure of the film. These pores have a uniform size distribution around 100 nm in diameter and 400 nm in length. The high-magnification SEM image of the sample shows the tubular structure more clearly (inset of Fig. 2a). Shown in Fig. 2b is a SEM image of the Ru-Pd BQDs (marked with arrows) deposited into TiO_2 NAs, indicating that well-ordered pores structure still exists, suggesting that the Ru-Pd BQDs deposition process does not damage the ordered TiO_2 NAs structure. We further studied the catalysts by TEM, which provided more important information (Fig. 2c). Obviously, on the surface of tubular structures, Ru-

Pd BQDs with a diameter of approximately 10 nm are homogeneously deposited. The uniform dispersion of Ru-Pd BQDs with a narrow size distribution over TiO_2 NAs suggests a rectifying Schottky barrier due to the formed Schottky junction as derived from the lattice anchoring interaction between Ru-Pd BQDs and the TiO_2 NAs support. In addition, the inset of Fig. 2c clearly shows the selected area electron diffraction pattern [44], indicating that the as-prepared samples are well-developed multiple crystal. Moreover, the compositions of the Ru-Pd BQDs was determined by energy dispersive X-ray spectroscopy (EDX) experiments (Fig. 2d). The EDX spectrum exhibits Ti, O, Ru, and Pd peaks, respectively (some overlapped signals for Ru, and Pd peaks around 2.6 keV). Ti and O peaks are regarded to be result from anatase TiO_2 , whereas Ru, and Pd peaks clearly reveal the presence of Ruthenium and Palladium element in the bulk of the TiO_2 NAs.

The crystal structures of anodized TiO_2 NAs and Ru-Pd BQDs/ TiO_2 NAs were characterized by XRD measurement as shown in Fig. S2. It can be seen from Fig. S2 that after anchoring Ru-Pd BQDs into titania NTs, the relative peaks intensities of XRD patterns of Ru-Pd BQDs/ TiO_2 NAs were partially decreased compared to that of naked TiO_2 NAs alone. This fact clearly revealed that Ru-Pd BQDs are successfully anchored and homogeneously dispersed onto the outer and inner surface of TiO_2 NAs [21]. It can be also observed from Fig. S1 that there are some strong XRD peaks of Ti substrate and a peak existed at $2\theta = 24.8^\circ$ corresponding to anatase TiO_2 (JCPDS No.21-1272), and no rutile TiO_2 phase was derived from composites preparation process, which might be beneficial for improving the PC activity as discovered in previously reports in comparison of Anatase and Rutile titania mediated reactions [45].

In order to fully elucidate and investigate the interfacial structure including chemical state of element and surface chemical compositions etc., the Ru-Pd BQDs/ TiO_2 NAs has now been analyzed by X-ray

photoelectron spectroscopy (XPS), and the whole XPS spectrum of Ti 2p, O 1s, Ru 3d and Pd 3d are depicted in Fig. S3(a), which obviously indicates the co-existence of Ti, O, Ru and Pd elements, respectively. The Ti 2p XPS discrete spectrum of the Ru-Pd BQDs/TiO₂ NAEs is displayed in Fig. S3b, and it is thought that the XPS peaks located at 464.7 and 459.1 can be assigned to Ti⁴⁺ 2p_{1/2} and Ti⁴⁺ 2p_{3/2}, respectively, which coincide perfectly with standard anatase TiO₂ (458.70 eV) indicating the formation of anatase TiO₂ in the aforementioned Ru-Pd BQDs/TiO₂ NAs composites. As displayed in Fig. S3c, the strongest peak centered at 286.7 eV can be attributed to C 1s standard background reference as taken in XPS runnings. The XPS isolated peak at 281.8 eV could be assigned to Ru 3d_{5/2}, which firmly confirmed the metallic state of Ru QDs and partial Ru species bearing low valence state Ru^{δ+} (0 < δ < 3). Accordingly, the XPS peaks centred at 340.6 eV (Pd 3d_{3/2}) and 335.3 eV (Pd 3d_{5/2}) are due to Pd QDs possessing Pd (0) states (see Fig. S3d) [46]. Furthermore, the XPS results of Ru-Pd BQDs/TiO₂ NAs composites confirm that the Ru/Pd is nearly 1.698: 1.580, imply that the Ru and Pd BQDs are uniform distribution on the nanocomposites with equal amount.

3.2. Charge carriers separation efficiency of Ru-Pd BQDs/TiO₂ NAEs

The PL characteristics of the as-prepared composites were studied to reveal interfacial charge transfer dynamics and mechanisms. Generally, the lowering of the emission intensity is indicative of a decrease in the radiative recombination and a high separation efficiency of electron–hole pairs [47]. For the pure TiO₂ NAEs, the two high-energy peaks centred at 395 and 445 nm could be assigned to surface recombination of the anatase TiO₂, while the peaks/shoulders centred at 380, 395, 484, 495 and 515 nm are induced by the presence of impurity energy level (Fig. 3a) [48]. After anchoring of TiO₂ NTEs with Ru-Pd BQDs, the surface recombination for the electrons and holes is quenched drastically, thus the decreased PL intensity is especially evident as reflected from the bands at 380–450 nm [49]. On the basis of these marvelous achievements, we therefore conclude that anchoring of TiO₂ NAEs with Ru-Pd BQDs can bring about highly efficient interfacial separations and segregations of photo-generated charge carriers [50].

Surface photovoltage spectroscopy (SPV) technique is conducted to further investigate the PECRD mechanism by revealing the kinetic behaviors of the photo-generated charge carriers [51]. Fig. 3b shows the whole SPV spectra of pure TiO₂ and Ru-Pd BQDs/TiO₂ samples. The pure TiO₂ presents an apparent SPV response ranging from 310 to 390 nm. This is representative feature of n-type semiconductor in SPV, where positive charges from inner semiconductor migrate to the surface [52]. Compared to the pure TiO₂, with the Ru-Pd BQDs coupling, the Ru-Pd BQDs/TiO₂ composites exhibit stronger SPV signals, indicating that the photo-generated e[−]/h⁺ pairs are separated more effectively and efficiently. It has been widely recognized that the increased SPV

intensity can be attributed to the efficient charge transfer between the interfaces of Ru-Pd BQDs and TiO₂ in the composite samples. More importantly, the SPV spectra coincide well with PECRD performance, which could further the fact i.e., the marvelous enhancement of separation efficiency of photo-generated electron–hole pairs is mainly caused by the Schottky-barriers as derived from the interfacial interaction within the Ru-Pd BQDs/TiO₂ NAEs metal-semiconductor composites bearing double Schottky-junctions.

3.3. Photoelectrocatalysis performance of Ru-Pd BQDs/TiO₂ NAEs

PEC measurements were performed in a three-electrode cell using Ru-Pd BQDs/TiO₂ NAEs as the working electrode with an exposed area of 4 cm² and 0.01 M Na₂SO₄ as the electrolyte. The photo-current density versus applied voltage scans of the samples were measured under UV light irradiation at 5 mW/cm² provided by a 300 W high-pressure mercury lamp. The results are presented in Fig. 4a. With the increase of the applied potential, the saturated photo-voltage of TiO₂ NAEs and Ru-Pd BQDs/TiO₂ NAEs are gradually enhanced and the photo-voltage of Ru-Pd BQDs/TiO₂ NAEs is 3.35 mA cm^{−2} at 1.0 V (vs. SCE) which is roughly 6.7 times higher than that of TiO₂ NAEs. Hence, a remarkably enhancement of PEC performance over Ru-Pd BQDs/TiO₂ NAEs composites was evidenced. The corresponding photo-conversion efficiencies are depicted and shown in Fig. 4b. As can be seen, Ru-Pd BQDs/TiO₂ NAEs yields the highest photo-conversion efficiency (14.10%) at −0.75 V in comparison with those of TiO₂ NAEs (0.45%) under identical parallel conditions. The marvelous enhancement of photo-conversion efficiencies can be attributed to the double Schottky-junctions as derived from the interfacial interaction within the Ru-Pd BQDs/TiO₂ NAEs metal-semiconductor composites, which would greatly facilitate the interfacial transfer of photo-induced charge carriers.

Furthermore, the time-dependent photocurrent of Ru-Pd BQDs/TiO₂ NAEs presents a well-correlated variation with the on/off cycles of UV light, and stable photocurrent density of about 0.60 mA cm^{−2} (Fig. 4c) has been attained which is approximate 6 times higher than that of pure TiO₂ NAEs (0.1 mA cm^{−2}). To gain deeper insight into the interfacial charge segregation and transfers, we have accomplished the electrochemical impedance spectra (EIS) characterization and the derived EIS spectra of Ru-Pd BQDs/TiO₂ NAEs composites was depicted and shown in Fig. 4d. In typical EIS Nyquist plots, semicircles in Nyquist plots of a semiconductor usually represents the charge-transfer process at the electrode/electrolyte interface and the radius of the semicircle partially imply the charge transfer resistance [53]. Under the complex conditions of applied bias and illuminations, the radius of the EIS semicircle for Ru-Pd BQDs/TiO₂ NAEs is much smaller than that of pure TiO₂ NAEs, which implicit the formation of Schottky barrier between Ru-Pd metals and TiO₂ semiconductors. The surface anchoring of Ru-Pd BQDs into Titania NTs bearing double Schottky-junctions caused dramatically

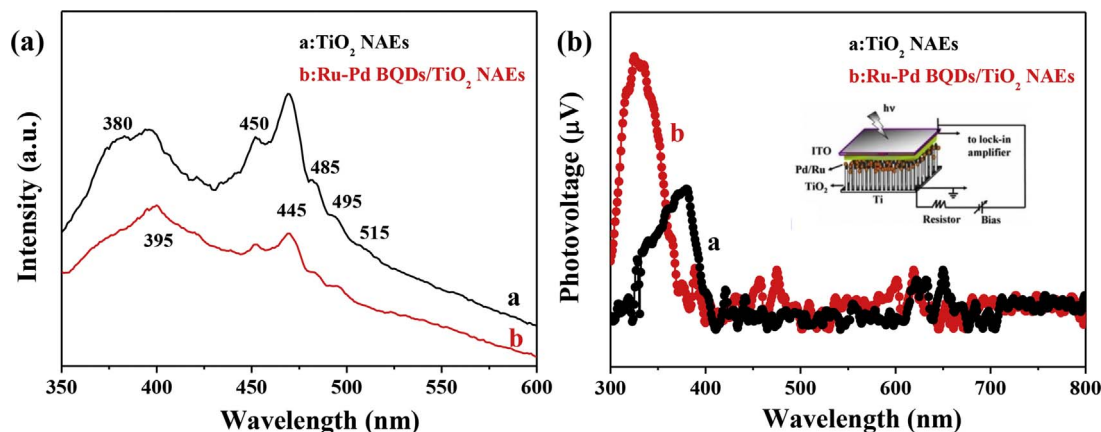


Fig. 3. (a) PL spectra and (b) SPV responses of the TiO₂ NAEs and Ru-Pd BQDs/TiO₂ NAEs.

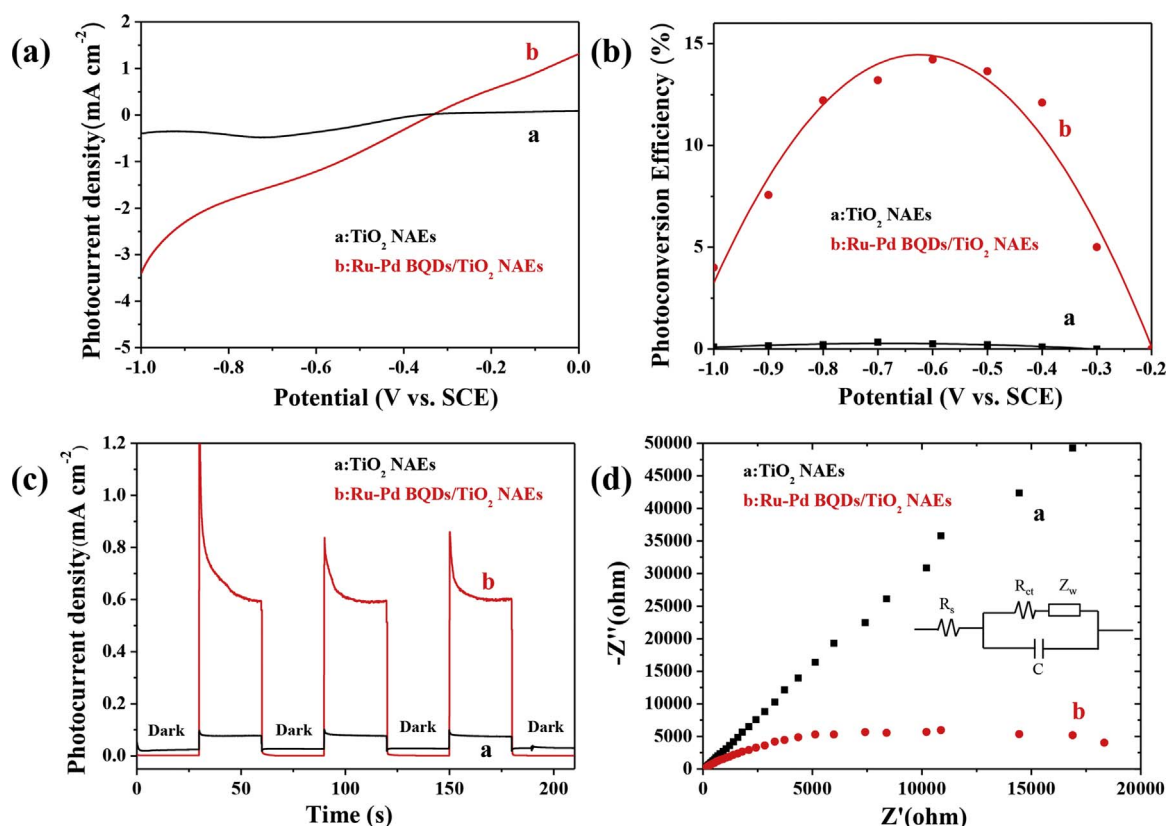


Fig. 4. (a) I-V characteristic, (b) the corresponding photoconversion efficiencies, (c) I-T characteristic and (d) the ac impedance spectra of the TiO_2 NAEs and Ru-Pd BQDs/ TiO_2 NAEs under UV light (5.0 mW cm^{-2}).

decrease in the EIS radius of arc compared with pure TiO_2 NAEs under light irradiations, suggesting that the Ru-Pd BQDs significantly increased the electron transfer between the electrolyte and the composite electrodes due to their excellent electrical conductivity, which would be beneficial for improving the interfacial charge segregation and transfer among Ru-Pd BQDs/ TiO_2 NAEs composites followed by enhancing their activities including photocatalysis, photoelectrochemical, PEC and PECRD process.

3.4. DFT calculation results

The catalytic activity of semiconductor mainly depends on the structures including crystal structure, electronic structures as well as gap energetics, which can be determined by using first principle analysis. As we know, TiO_2 (101) is rather chemical stable than TiO_2 (001), DFT calculations were then carried out to deeply investigate the crystal and electronic structures of Ru-Pd BQDs/ TiO_2 NAEs. The most stable grafting and/or anchoring sites for single Pd or single Ru adatoms as

adopted in this research is based on previously reports [39,40] (Fig. 5). It is well established that the bridge sites formed by two-coordinated oxygen (O_{2c}) atoms at the step edge were most stable for single Pd or Ru anchoring. Following up this issue, the well-defined eight configuration structures of Ru and Pd bimetal adatoms on the anatase TiO_2 (101) surface were systematically investigated to model the Schottky barriers, denoted as Ru-Pd_(n)/ TiO_2 (101) ($n = 1, 2, \dots, 8$), respectively. In the first four configuration structures (Fig. 6a–d), the Pd atoms are kept grafting at the most stable 2cO-bridge site, while Ru atoms are located on the $\text{Ti}_{5c}\text{-O}_{3c}$ bridge site, $\text{O}_{2c}\text{-Ti}_{6c}\text{-O}_{3c}$ bridge site and $\text{O}_{3c}\text{-Ti}_{5c}$ bridge site, respectively. In addition, it can be seen that the bond lengths of Ru-Pd as derived from the top configuration structure of O_{3c} are 2.57, 2.93, 2.55 and 2.56 Å respectively. Ru-Pd₍₅₎ and Ru-Pd₍₆₎ (Fig. 6e–f) are accordingly obtained by arranging the adatoms at $\text{O}_{2c}\text{-Ti}_{5c}$ bridge site and $\text{O}_{2c}\text{-Ti}_{5c}\text{-O}_{3c}$ bridge site with the same Ru–Pd bond lengths of 2.60 Å. Furthermore, the other two configuration structures are well constructed by grafting both of the Pd atom to the most stable single Ru grafting, which would induce the stable structures including Ru-Pd₍₇₎

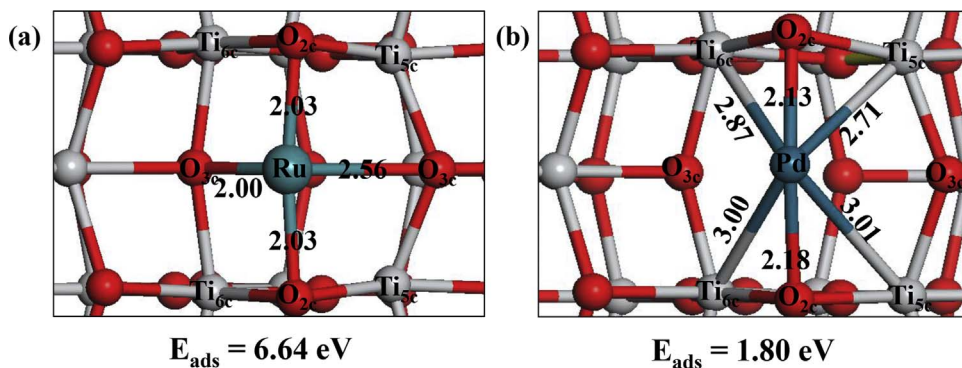


Fig. 5. The stable structures of a single Ru adatom (a) and Pd adatom (b) on anatase TiO_2 (101) surface.

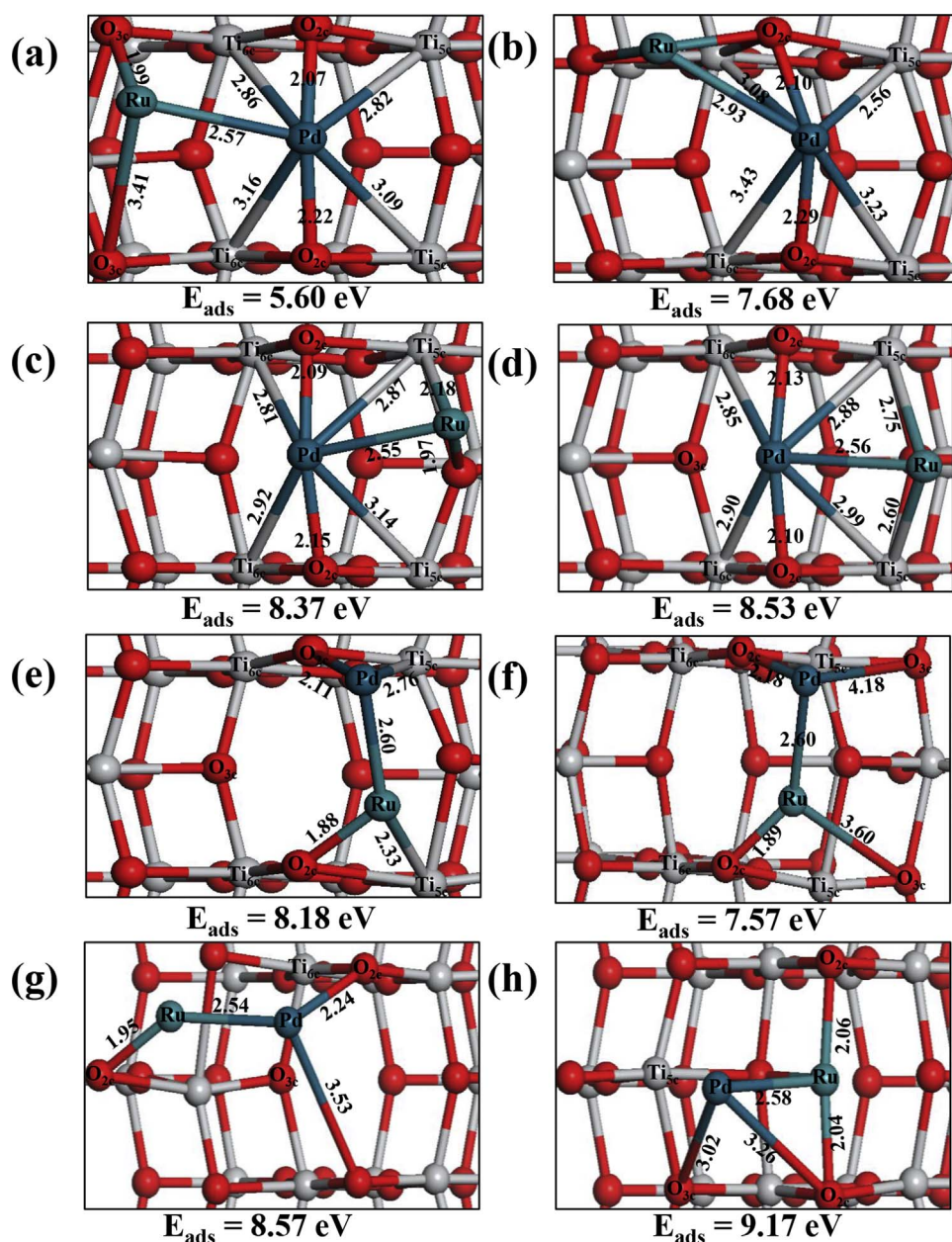


Fig. 6. Relaxed structures of single Ru and Pd adatoms on anatase TiO_2 (101) surface: (a) Ru-Pd₁, (b) Ru-Pd₂, (c) Ru-Pd₃, (d) Ru-Pd₄, (e) Ru-Pd₅, (f) Ru-Pd₆, (g) Ru-Pd₇, (h) Ru-Pd₈.

and Ru-Pd₍₈₎ (Fig. 6g–h) with the Ru–Pd bond lengths became 2.54 and 2.58 Å, respectively.

To gain deeper insight into the interface property of Ru-Pd BQDs/ TiO_2 NAEs, the adsorption energy as well as the binding energy etc. have been calculated (Fig. 7). The energy bands, adsorption energy, binding energy of TiO_2 , Ru/ TiO_2 , Pd/ TiO_2 and Ru-Pd_(n)/ TiO_2 (101) ($n = 1, 2, \dots, 8$) are illustrated in Table S1. As referred from the outcomes of DFT calculations, it can be drawn that the most stable configuration structure on the TiO_2 (101) surface has been determined to be Ru-Pd₍₈₎ with the highest E_{ads} of 9.17 eV. And the adsorption energies of the Ru-Pd_(n) ($n = 1-7$) are 5.60, 7.68, 8.37, 8.53, 8.18, 7.57 and 8.57 eV, respectively, which are much different from that of Ru/ TiO_2 and Pd/ TiO_2 (6.64 and 1.80 eV, respectively). Additionally, it is found that Ru-Pd_(n) ($n = 3-7$) are energetically close, demonstrating that the different active sites for Ru and Pd atoms surface anchoring became very competitive. Therefore, we accordingly elucidated the binding energy between Ru and Pd to check the defined stability of the two atoms simultaneously anchoring onto the surface of TiO_2 (101). Obviously, the binding energies of 4.95 eV for Ru-Pd₍₈₎ is found to be

superior to that of Ru-Pd_(n) ($n = 1-7$) (3.39, 3.47, 3.60, 3.76, 3.41, 3.35 and 3.80 eV, respectively). The results further illustrated that, although the O_{2c} -bridge site is the most active for Pd or Ru monomer, the Ru-Pd bimetal cannot simultaneously occupy two of them. While the Pd-Ru bimetal atoms anchored on the TiO_2 (101) surface, it will consider not only the activity of the adsorption sites but also the distance between the two sites. Therefore, both of the 2cO-6cTi-3cO bridge sites and the 2cO-bridge sites became more competitive during the Ru-Pd bimetal atoms adsorption than that in a single Pd or Ru surface derivations.

To further understand the electronic structure of the single atoms on the surface of anatase TiO_2 (101), the total densities and partial density of states (PDOS) for the clean TiO_2 (101) surface as well as different metal-support interaction systems were calculated (Fig. 8). The energy zero (i.e., the Fermi energy level, EF) is set at the valence band maximum (VBM) in every system. In the case of pure TiO_2 (101), the valence and conduction states are mainly derived from the O 2p orbitals and the Ti 3d orbitals, respectively, with the calculated band gap of ~ 2.067 eV. This value is lower than the experimental data (3.18 eV) because of the underestimation of band gap by the PBE functional (Fig.

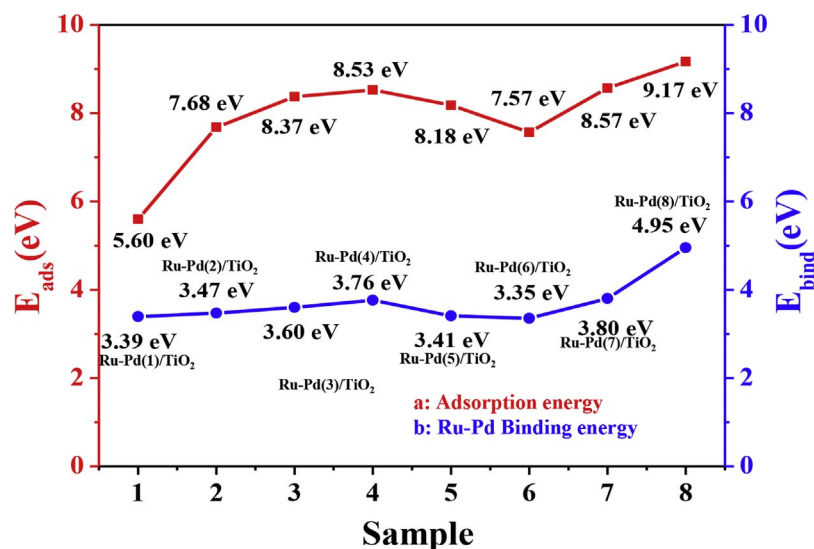


Fig. 7. The adsorption energy and binding energy of Ru-Pd_(n)/TiO₂(101) (n = 1, 2, ...8).

S4). As a result of the introduction of Ru and Pd QDs, some isolated energy bands can be found which led to the composites showing multiband characteristics. Since the lower isolated energy band is close to the top of the valence band (VB) for each system, the relative distance between them is 0.72, 0.22, and 0.22 eV for Ru/TiO₂, Pd/TiO₂ and Ru-Pd BQDs/TiO₂ (101), respectively (Fig. S5). For the upper isolated energy band, its relative distance to the bottom of the conduction band (CB) is the smallest in Ru-Pd BQDs/TiO₂ (101) (0.50 eV). Compared with mono-grafted systems, in the Ru and Pd bimetal grafting systems, the number of impurity energy levels increased and some were overlapped with original energy level which promoting electron energy transition and finally reduce the excitation energy. Additionally, there are some metal induced gap states (MIGS), as shown in Fig. 8(e)–(g). For the PDOS of the Ru-TiO₂, Pd-TiO₂, Ru-Pd BQDs/TiO₂, the region close to the Fermi level (−2 to 2 eV) has Ru and/or Pd metallic characters, indicating that MIGS are entirely arising from supported Ru and/or Pd QDs. Although in Ru-TiO₂ (2.100 eV), Pd-TiO₂ (2.119 eV), Ru-Pd BQDs/TiO₂ (2.111 eV) composites, the band-gap was calculated to be a little larger than that of the pure TiO₂ (2.067 eV), it is possible to excite electrons from the VB to the intermediate energy levels by using

lower energy light than that needed for the pure TiO₂. The intermediate energy levels offer additional steps for the absorption of low energy photons through the excitation of VB electrons to these intermediate energy levels, from where they can be excited again to the CB [54]. These calculated results indicate that the Ru-Pd₍₈₎/TiO₂ (101) composite systems will present more light absorption for the lower energy photon. All Pd or Ru 4d orbitals are incompletely filled, with states spilling across the Fermi level. This should make the redistribution of charges into different d orbitals easier, and hence, it should make the Pd and Ru atoms more polarizable. Therefore, the significant intermediate impurity bands permit enhanced carrier separation, as mobile electrons of various energetic states within them can offer enhanced electron conductivity together with improved optical absorption [39,55]. As we know, when a metal and semiconductor come into contact, a redistribution of electric charge occurs and the Fermi levels of the two materials align until a thermodynamic equilibrium is reached at the metal-semiconductor interface, forming a type of junction. The alignment results in an upward bending of both the VB and the CB, and the formation of a Schottky barrier between the semiconductor and the metal [56]. The degree of band bending is dependent on the work

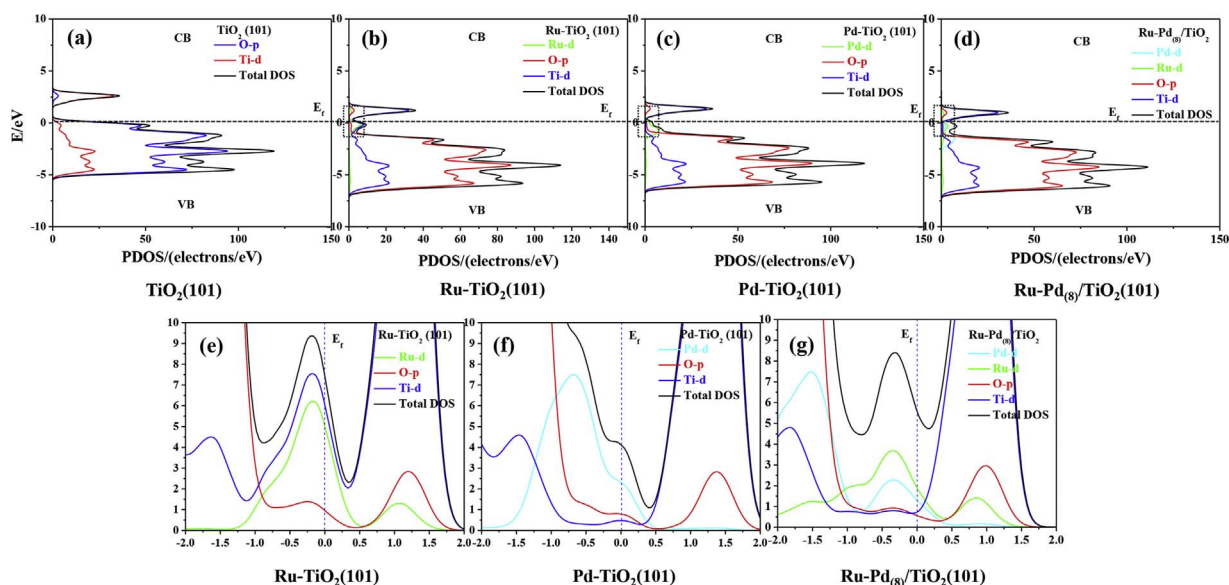


Fig. 8. Partial density of states of (a) clear TiO₂ (101), (b) Ru/TiO₂, (c) Pd/TiO₂ and (d) Ru-Pd BQDs/TiO₂ systems (E_f – Fermi energy level). The partial magnification diagrams of DOS on the Fermi level of the Pd/TiO₂, Ru/TiO₂ and Ru-Pd BQDs/TiO₂ systems are marked as (e), (f) and (g), respectively.

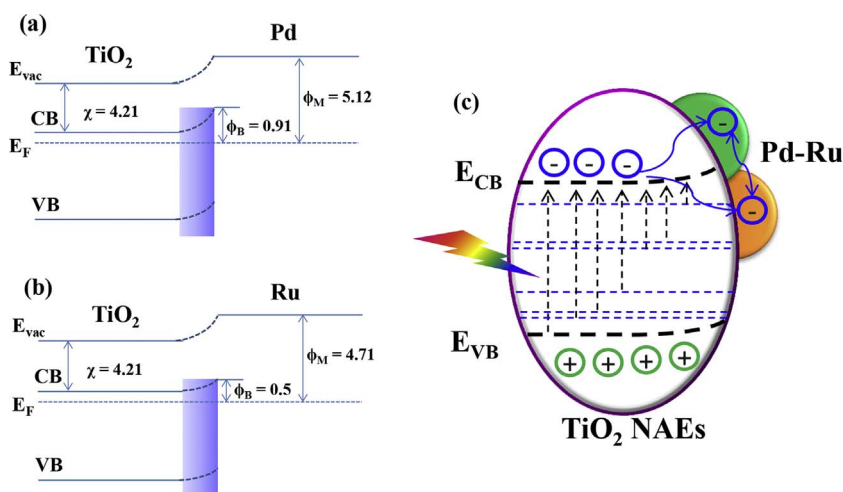


Fig. 9. (a) Formation of Schottky barrier at the Pd/TiO₂ interface (a) and at the Ru/TiO₂ interface (b) where χ is the electron affinity of TiO₂, Φ_B is the barrier height and Φ_M is the work function of the metal. (c) Proposed mechanism of the Ru-Pd BQDs/TiO₂ bimetal-support interaction. (The blue lines represent the impurity energy levels). (For interpretation of the references to colour in this figure legend, the reader is referred to the web version of this article.)

function of the metal and the electron affinity of the semiconductor, and this determines the ultimate height of the barrier formed and indicates whether the metal nanoparticle can inhibit the recombination of excited charge carriers by acting as an electron or a hole traps [57]. The barrier height, Φ_B was calculated using Eq. (3.1) [58].

$$\Phi_B = \Phi_M - \chi \quad (3.1)$$

The Φ_M value of Pd is 5.12 eV and Ru is 4.71 eV which is cited from the reference [59]. The χ of TiO₂ estimated at 4.21 eV [57]. The Φ_B was calculated to be 0.91 eV for Pd/TiO₂ and 0.5 eV for the Ru/TiO₂ photocatalyst as shown in Fig. 9a and b, respectively, suggesting that Pd and Ru BQDs can act as electron traps. The results imply that surface derivation including anchoring of bimetal-semiconductor composites could incur an up band bending and a double Schottky barrier, which will significantly promote the interfacial charge carriers separation and transfers. Lower energy photons could excite electrons from the valence band to the conduction band by the impurity energy levels, which will significantly promote the visible light adsorption. Therefore, by referring to the afore-mentioned elucidations, we can then assume that when the composites of Ru-Pd BQDs/TiO₂ NAEs are irradiated, the excited electrons would transfer from VB of semiconductor TiO₂ to these doping-levels or from one doping-level to CB of TiO₂ easily, and then transfer to the metals through the Schottky barriers (Fig. 9c). Meanwhile, the generated electrons in the CB of TiO₂ are more difficult to move back from CB to VB, which prevents the corresponding recombination more efficiently [60]. The exciting behavior of improved interfacial electron transfer is further elucidated by electronic density

difference (EDD) integrations and analysis (shown in Fig. 10). Compared with TiO₂(101) (Fig. 10a), the EDD of Ru-Pd BQDs/TiO₂ NAEs composites (Fig. 10b) shows that the Pd-2cO and Ru-2cO bonds are greatly polarized in which electrons move away between the Ru/Pd atoms and the surface O atom. The depletion of electron density from Pd and Ru adatoms significantly reduces the Pauli repulsion that the metal atom experienced and leads to a stronger attractive interaction at the Ru-Pd BQDs/TiO₂ NAEs interface. More specifically, either Ti–Ru or Ti–Pd bond cannot be generated and observed in the composites, which indicates that the interface of the afore-mentioned bimetal–semiconductor is predominantly composed of Ru–O and Pd–O bonds, with the absence of metallic Ti–Ru or Ti–Pd bond in the composites.

3.5. Photoelectrocatalytic reductive dechlorinations activity

Before, detected the PECRD activity of as-synthesized composites, the adsorption of PCP on the Ru-Pd BQDs/TiO₂ NAEs under dark were studied (Fig. S6). The results displayed that the adsorption property is not the key fact for the PECRD process. Firstly, we compare the PECRD capability of the TiO₂ NAEs and Ru-Pd BQDs/TiO₂ NAEs for PCP elimination. It is clearly evidenced from Fig. 11a that the TiO₂ NAEs and Ru-Pd BQDs/TiO₂ NAEs exhibited total different PEC activities. The PECRD efficiency of PCP over Ru-Pd BQDs/TiO₂ NAEs is faster than that of pure TiO₂ NAEs alone. The PECRD enhancement was mainly attributed to double Schottky-junctions as derived from the interfacial interaction within the Ru-Pd BQDs/TiO₂ NAEs metal-semiconductor composites, which would greatly facilitate the interfacial transfer of photo-induced charge carriers following by fully utilization of the

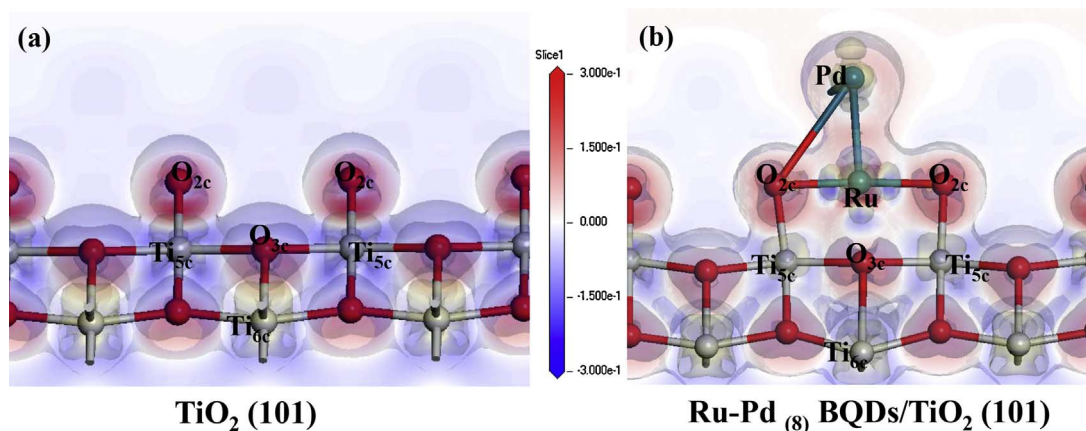


Fig. 10. Electronic deformation density of pure TiO₂ and Ru-Pd₈ BQDs/TiO₂ NAEs. Red and blue regions indicate the electron depletion and accumulation, respectively (cyan, Pd; loden, Ru; red, O; white, Ti). (For interpretation of the references to colour in this figure legend, the reader is referred to the web version of this article.)

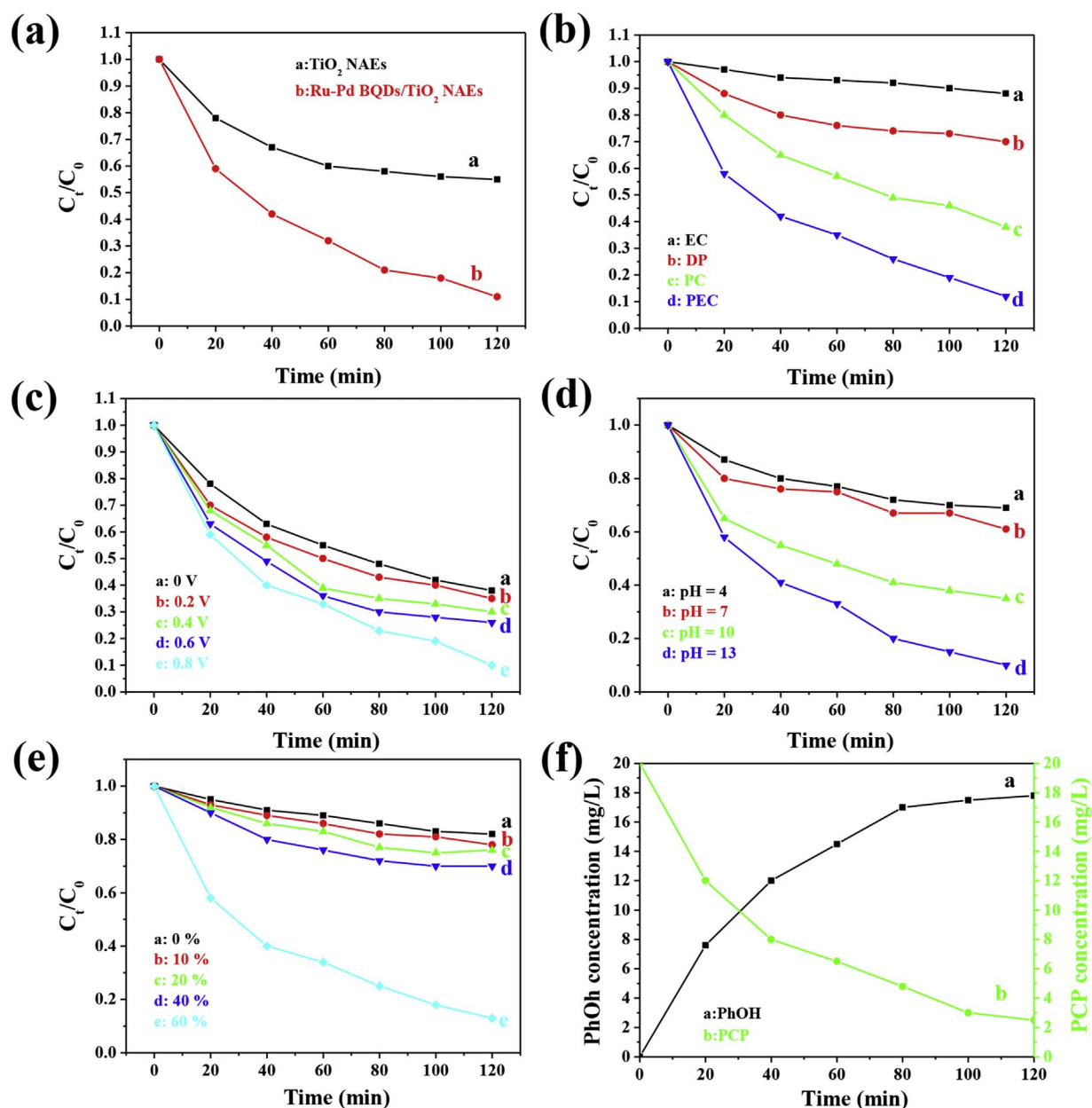


Fig. 11. PCP degradation of (a) different electrodes, (b) electrochemical (EC); direct photolysis (DP); photocatalysis (PC); photoelectrocatalytic reductive dechlorinations (PECRD). (initial concentration = 20 mg/L, applied bias potential = 0.6 V, light intensity = 5.0 mW/cm²); (c) The PECRD of PCP by different bias potential (0 V; 0.2 V; 0.4 V; 0.6 V; 0.8 V), (d) different pH (pH = 13; pH = 10; pH = 7; pH = 4), (e) different water capacity (0%; 10%; 20%; 40%; 50%) and (f) Change in the concentration of PCP and PhOH during the PECRD of PCP.

Table 1
Pseudo-first-order rates of PCP degradation under different process.

Method	k (min ⁻¹)	R ²
Electrochemical	0.0016	0.9806
Direct photolysis	0.0034	0.9062
Photocatalysis	0.0097	0.9264
Photoelectrocatalysis	0.0194	0.9475

photo-generated electrons for PECRD of PCP species.

Systematical and chronicle experiments including Electrochemical (EC), Direct Photolysis (DP), PC and PECRD degradation of PCP species have been carried out for the sake of checking the apparent variations of PCP degradation efficiencies among four individual processes. The variations of relative concentration of PCP (C_t/C_0) as a function of reaction time was dictated and shown in Fig. 11b. Almost no PCP removal

was observed in the EC process under 0.6 V (vs. SCE) bias potential. Direct UV irradiation degraded 33.86% of the PCP in 2 h. Compared to DP, the Ru-Pd BQDs/TiO₂ NAEs photoelectrocatalytic reductive degradation of PCP reached 90.25% within the same duration time. Obviously, it can be drawn from the afore-outcomes that the catalytic degradation rate of PCP was the largest for PECRD process with the identical and parallel conditions including the same bias potential and ultraviolet light intensity etc.

It has been well recognized from tremendous reports that the PECRD degradation of organic pollutants follows pseudo-first-order kinetics [61]. Herein, pseudo-first-order kinetics was also double confirmed in the four processes by the linear transform of $\ln(PCP_0/PCP_t) = kt$ (k is the kinetic constant). As shown in Table 1, the pseudo-first kinetic constant of PECRD for PCP degradation process is larger than the total sum of the EC and PC processes individually. Thus, it is reasonable to conclude that a sort of synergistic effect occurs during the

PECRD of PCP species.

Bias potential is one of the most predominant factors that influences PECRD efficiency, which has been thought to favor the interfacial electron transfers as derived from photo-generated charge carriers among Ru-Pd BQDs/TiO₂ NAEs composites with double Schottky-barriers. Herein, the positive effect of the bias potential on the PECRD degradation rate of PCP was further checked and elucidated. As seen in Fig. 11c, it is clearly shown that the degradation rate of PCP was increased from the bias potential of 0 V to 0.8 V followed by approaching the largest value at the bias potential of 0.6 V as 90.25% of PCP was degraded in 2 h, whereas it was only 68.9% without bias potential supply. In this case, there is a sort of synergetic effect occurs during the PECRD of PCP species. The external applied bias potential supplied to the Ru-Pd BQDs/TiO₂ NAEs contributes to the spatial effective charges segregation and transfer of the photo-generated electrons and the holes. The charge segregation and transfer would then greatly retard the subsequent recombination of photo-generated hole-electron pairs. Hence, the electrons as derived in this situation would have more opportunities to participate in the light induced redox processes and catalytic degradation reactions. Consequently, the degradation efficiency increases. However, with the higher bias potential, the effect of degradation decreases which is due to the number of photo-generated electrons is pretty finite under a fixed light intensity with regard to a certain thickness of TiO₂ NTs. Therefore, the saturation current could be incurred while bias potential reached a certain value, the PECRD degradation efficiency would reach a platform without bearing more opportunity for further being raised. In fact, this phenomenon was pretty similar to that reported by Zhao et al. [62]. Hence, it can be inferred that the supplied bias potential has an optimal value to some extent under specific reaction conditions.

On the other hand, the pH value of solution is a common factor that influences fully removal of pollutants in many chemical reaction processes. The efficiency dependence of PECRD for PCP on the specific pH value of the solution was systematically checked and elucidated under the constant bias potential of 0.6 V and UV light intensity of 5.0 mW/cm² situations (Fig. 11d). The efficiency of PECRD degradations was found to be marvelously enhanced in an alkaline medium. Whereas, whilst in acid solution with pH value of 4, the catalytic decomposition rate of PCP was about half of that in basic solution with pH value centred at 13. Since NaOH was soluble in 2-propanol and sodium chloride (NaCl) was not, these results indicate that chloride ions eliminated from PCP were solidified with NaOH as NaCl. In addition, Dolfing et al. [63] has reported that higher pH value is of benefit to the reductive dechlorination of PCP due to the higher Gibbs free energy yield. Besides, based on the energy band theory, the basic surrounding environment is very beneficial to the photocatalytic reduction, whereas the acid surrounding environment is good for photocatalytic oxidation [64]. Obviously, in our case, the PECRD of PCP favored the basic surrounding reaction environment, which might be due to the intrinsic reductive degradation mechanism of PCP instead of the PEC oxidation pathways.

Water capacity is also an important factor that influences PECRD degradation of PCP species, and one could observe that while 10% water was added to the solution, the catalytic degradation of PCP was remarkably suppressed (Fig. 11e). Obviously, it can be concluded from the afore-performed experimental outcomes that the PECRD degradation of PCP greatly depends on the crystal and electronic structures as well as interface characteristics of Ru-Pd BQDs/TiO₂ NAEs. Interestingly, we found that whilst in 2-propanol-H₂O, where the adsorption of PCP species was weak, the catalytic degradation scarcely occurred. In general, the PECRD reaction primarily occurs on the surface of catalytic materials, and the pre-adsorption affects the accessibility of the surface reducing species to the PCP and the reduction kinetics. Moreover, the presence of water can form $\cdot\text{OH}$ radicals under specific conditions, which will have the tendency to incur the catalytic reduction environment. Fig. 11f shows the PEC dechlorination of PCP in 2-propanol

solution with supplying the external constant bias potential of 0.6 V containing NaOH under irradiation of ultraviolet light. PCP was almost fully consumed within 120 min time range and working conditions, and specific phenol was formed with a high stoichiometry during the PECRD processes, indicating that almost complete dechlorination of PCP was achieved under the current working conditions by using Ru-Pd BQDs/TiO₂ NAEs composites bearing Schottky-barriers as catalytic materials. Furthermore, the mineralization of PCP is analyzed by measuring the total organic carbon (TOC) concentration taken at regular time intervals (Fig. S7). In EC process, only 12% mineralization efficiency is achieved but it significantly enhances up to about 67% for PEC reaction. This can be rationalized by the synergistic effect between PC and EC. This result confirms that PECRD is most efficient reaction than PC, EC and DP for the PCP degradation.

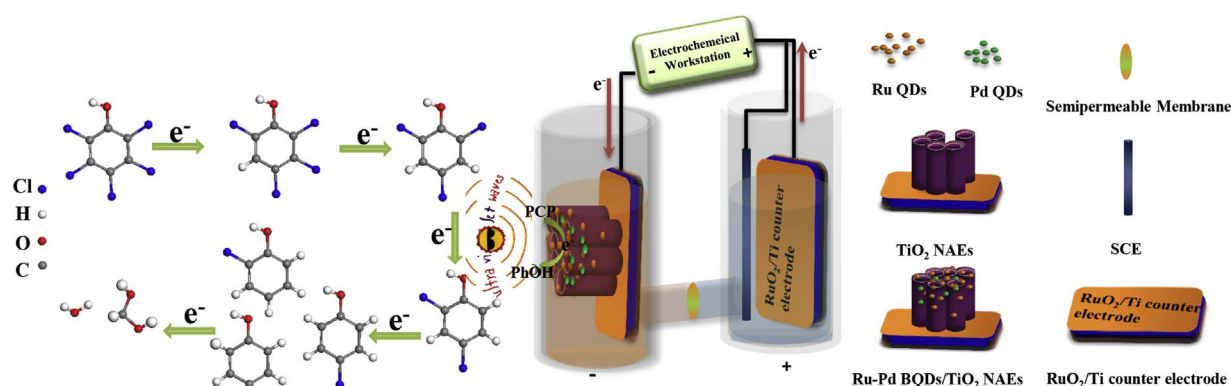
3.6. Photoelectrocatalysis degradation mechanism

In order to have a deeper understanding for the PECRD of PCP mechanism, besides of the afore-employed physical techniques for systematical characterization the physic-chemical characteristics of composites catalytic materials, electron spin resonance (ESR) DMPO-capture and time-resolved emission spectra (TAS) technology are used to reveal the generated active species ($\cdot\text{OH}$ and $\text{O}_2\cdot^-$) and the kinetic mechanisms of charge carrier transfer processes in the catalytic reaction. After illumination, there is no distinct ESR peaks of the DMPO- $\cdot\text{OH}$. While as shown in Fig. S7a, characteristic signals of the DMPO- $\text{O}_2\cdot^-$ are detected, indicating that $\text{O}_2\cdot^-$ was generated after light irradiation and was the main active species in the reaction. Generally, in the PEC reaction, $\text{O}_2\cdot^-$ is generated from O_2 reacted with e^- , thus, it is further confirmed that more electrons were generated by the illuminated of the Ru-Pd BQDs/TiO₂ composites and reacted with e^- to generate $\text{O}_2\cdot^-$ active species for highly efficient PECRD process. Additionally, the signal intensity is much higher in Ru-Pd BQDs/TiO₂ NAEs than in pure TiO₂ NAEs indicating the fast charges separation in the as-synthesized double schottky-barriers. Furthermore, compared to the normalized time traces of TiO₂ NAEs (Fig. S7b and c), the photo-generated holes in Ru-Pd BQDs/TiO₂ NAEs display a much longer lifetime (70.51 μs) than that of pure TiO₂ NAEs (50.51 μs). This demonstrates that Ru-Pd BQDs double Schottky-junctions could effectively prolong the lifetime of photogenerated charges, leading to the higher photocurrent for Ru-Pd BQDs/TiO₂ NAEs.

More importantly, LC-MS spectrometer were used to further identify and elucidate the PECRD reactions. Fig. S10 illustrates the total ion chromatogram and mass spectra of peaks a, b, c, d and e obtained from the PCP degradation over Ru-Pd BQDs/TiO₂ NAEs (initial concentration of PCP = 20 mg/L, bias potential = 0.6 V and UV light intensity = 5.0 mW/cm²). Many peaks at different intensities have been observed and identified, which obviously indicated the variations in the composition and concentration of the degradation products. A signal at $m/z = 264$ suggested the substrate PCP species. Furthermore, these species could be PEC dechlorinated i.e., PECRD consecutively to form chlorine-free intermediates and non-toxic species, including 4-chlorophenol ($m/z = 231$), trichlorophenol ($m/z = 197$), 2,4-dichlorophenol ($m/z = 163$), 2-chlorophenol and 4-chlorophenol ($m/z = 126$) and carbon dioxide, respectively. The detail mechanism of PECRD degradations of PCP over Ru-Pd BQDs/TiO₂ NAEs composites in chronically order has been proposed and depicted in Scheme 1, which would provide a brand new insight into the catalytic dechlorination pathways for typical environmental toxic polychlorinated compounds over multifunctional nanocatalytic materials.

3.7. Stability studies

We also used SEM, TEM and XPS to characterize the composition of the as-synthesized composites after PECRD process (Figs. S9 and S10). After catalysis reaction the morphology of the Ru-Pd BQDs/TiO₂ NAEs



Scheme 1. Possible mechanism of degradation pathways of PCP.

did not change significantly. A slightly changed distribution of Pd-Ru nanoparticles in some areas probably due to the detached outermost Pd-Ru cocatalyst being incorporated into the electrolyte solution. It demonstrated that the deposition of Pd-Ru BQDs on TiO₂ NTs not only enhanced the photocurrent density for the PECRD reaction but also appreciably preserved the photocatalytic stability of the Ru-Pd BQDs/TiO₂ NAEs.

4. Conclusions

In this work, novel palladium (Pd) and ruthenium (Ru) Bimetal Quantum Dots (BQDs) co-anchored on Titania nanotube arrays electrodes (NAEs) bearing double Schottky junctions with superior green energy conversions and environmental elimination properties have been successfully designed and prepared by facial two-step electrochemical strategy. To deeply investigate the nature of the promoted polychlorinated compounds by the photoelectrocatalytic reduction performance over Ru-Pd BQDs/TiO₂ NAEs composites, the PCP degradation was chosen as probe reaction under different reaction conditions including various bias potential, the presence of H₂O, acids and/or bases etc. A remarkable enhancement of photoelectric conversion performance (14.10%) as compared to that of the pure TiO₂ NAEs (0.45%) in the Ru-Pd BQDs/TiO₂ composites bearing double Schottky-barriers. PCP could be fully dechlorinated to a chlorine-free product at 0.6 V bias potential in 2-propanol solution in the presence of NaOH under irradiation of ultraviolet light. Moreover, the PECRD elimination efficiency of PCP has been successfully approaching to above 90% under UV light irradiation conditions. Obviously, significant promotion both of the PECRD catalytic activity of Ru-Pd BQDs/TiO₂ NAEs toward PCP reduction and energy conversion have been obtained, which is mainly due to the specific crystal-, electronic and micro-interfacial structures of the composites with double Schottky junction as verified by various combined techniques including UV-vis spectroscopy, XRD, SEM/TEM/EDX, PL, EIS, SPV and XPS etc. It is further pointed out that marvelous enhancement of separation efficiency of photo-generated electron-hole pairs is mainly caused by the Schottky-barriers as derived from the interfacial interaction within the Ru-Pd BQDs/TiO₂ NAEs metal-semiconductor composites bearing double Schottky-junctions, which would greatly facilitate the interfacial charge transfer followed by fully utilization of the photo-generated electrons for PECRD of PCP species. Furthermore, first principles DFT calculations results indicated that the growth of Ru and Pd bimetal atoms at the anatase TiO₂ (101) surface is mainly driven by the interaction between Ru/Pd and surface atoms, and the most active site for bimetal Ru and Pd adatoms on the perfect TiO₂ (101) surface is the 2cO-6cTi-3cO bridge sites and the 2cO-bridge sites with the highest adsorption energy of 9.17 eV. What's more, the outcomes of electronic calculations demonstrating that in the Ru-Pd bimetal-semiconductor composites with double Schottky junctions, the number of impurity (i.e., co-anchored Ru-Pd BQDs) energy levels

increased and some were overlapped with original energy level, promoting electron energy transition and reduces the band gap. Besides, the surface derivation including anchoring of bimetal BQDs into Titania NTs could incur an up band bending and a double Schottky barrier promoting electron energy transition and reduces the band gap, which will significantly promote the interfacial charge carriers separation and transfers. Hence, whilst the composites of Ru-Pd BQDs/TiO₂ NAEs were irradiated under ultraviolet light, the excited electrons would transfer from VB of semiconductor TiO₂ to these mid-levels or from one mid-level to CB of TiO₂ easily, and then transfer to the metals through the Schottky barriers. Meanwhile, the generated electrons in the CB of TiO₂ are more difficult to move back from CB to VB, which prevents the corresponding recombination more efficiently.

The detail mechanism of PECRD degradations of PCP over Ru-Pd BQDs/TiO₂ NAEs composites in chronically order were further integrated and elucidated by LC-MS in combination with the aforementioned physico-chemical characterizations and DFT theoretical calculations, which could significantly deepen our understanding to the catalytic dechlorination pathways of typical environmental toxic polychlorinated compounds over multifunctional nanocatalytic materials. Overall, the experimental outcomes here indicated that Ru-Pd BQDs/TiO₂ NAEs composites with double Schottky junctions possess superior performance both for photoelectrochemical conversion and photoelectrocatalytic dechlorination of polychlorinated compounds, which would be very beneficial for molecular design designing efficient light harvesting nanomaterials with marvelous activity, stability and recyclability towards highly efficient environmental eliminations and green energy conversions both at fundamental and practical level.

Acknowledgements

This work was supported financially by the Major Program of the National Natural Science Foundation of China (No. 21590813), the National Natural Science Foundation of China (Nos. 21377015 and 21577012), the Key Project of the National Ministry of Science and Technology (No. 2016YFC0204204), the Program of Introducing Talents of Discipline to Universities (B13012), and the Key Laboratory of Industrial Ecology and Environmental Engineering, China Ministry of Education.

Appendix A. Supplementary data

Supplementary data associated with this article can be found, in the online version, at <https://doi.org/10.1016/j.apcatb.2018.01.043>.

References

- [1] L.K. Weavers, N. Almstadt, M.R. Hoffmann, *Environ. Sci. Technol.* 34 (2000) 1280–1285.

- [2] K. Govindan, M. Raja, M. Noel, E.J. James, J. Hazard. Mater. 272 (2014) 42–51.
- [3] X. Zhang, Y. Tang, Y. Li, Y. Wang, X. Liu, C. Liu, S. Luo, Appl. Catal. A Gen. 457 (2013) 78–84.
- [4] Q. Fang, X. Shi, L. Zhang, Q. Wang, X. Wang, Y. Guo, B. Zhou, J. Hazard. Mater. 283 (2015) 897–904.
- [5] S. Zhang, H. Yang, H. Gao, R. Cao, J. Huang, X. Xu, ACS Appl. Mater. Interfaces 9 (2017) 23635–23646.
- [6] K. Fukui, K. Hashimoto, H. Kominami, Chem. Commun. 46 (2010) 5118–5120.
- [7] L. Yin, J. Niu, Z. Shen, J. Chen, Environ. Sci. Technol. 44 (2010) 5581–5586.
- [8] J.F. Callejas, o.M. McEnaney, C.G. Read, J.C. Crompton, A.J. Biacchi, E.J. Popczun, T.R. Gordon, N.S. Lewis, A.R.E. Schaak, ACS Nano 8 (2014) 11101–11107.
- [9] J.L. White, M.F. Baruch, J.E. Pander Iii, Y. Hu, L.C. Fortmeyer, J.E. Park, T. Zhang, K. Liao, J. Gu, Y. Yan, T.W. Shaw, E. Abelev, A.B. Bocarsly, Chem. Rev. 115 (2015) 12888–12935.
- [10] H. Yang, S. Zhang, R. Cao, X. Deng, Z. Li, X. Xu, Sci. Rep. 7 (2017) 8686.
- [11] R. Li, Y. Weng, X. Zhou, X. Wang, Y. Mi, R. Chong, H. Han, C. Li, Energy Environ. Sci. 8 (2015) 2377–2382.
- [12] W. Zhou, H. Liu, J. Wang, D. Liu, G. Du, J. Cui, ACS Appl. Mater. Interfaces 2 (2010) 2385–2392.
- [13] B. Tapin, F. Epron, C. Especel, B.K. Ly, C. Pinel, M. Besson, ACS Catal. 3 (2013) 2327–2335.
- [14] S. Zhang, H. Gao, J. Li, Y. Huang, A. Alsaedi, T. Hayat, X. Xu, X. Wang, J. Hazard. Mater. 321 (2017) 92–102.
- [15] Q. Zhao, D. Ju, X. Deng, J. Huang, B. Cao, X. Xu, Sci. Rep. 5 (2015) 7874.
- [16] S. Bai, W. Yin, L. Wang, Z. Li, Y. Xiong, RSC Adv. 6 (2016) 57446–57463.
- [17] M. Chen, Y. Zhang, L. Xing, Y. Liao, Y. Qiu, S. Yang, W. Li, Adv. Mater. 29 (2017) 1607015.
- [18] Y.C. Nah, I. Paramasivam, P. Schmuki, ChemPhysChem 11 (2010) 2698–2713.
- [19] Y. Xia, P. Yang, Y. Sun, Y. Wu, B. Mayers, B. Gates, Y. Yin, F. Kim, H. Yan, Adv. Mater. 15 (2003) 353–389.
- [20] X. Dai, Z. Zhang, Y. Jin, Y. Niu, H. Cao, X. Liang, L. Chen, J. Wang, X. Peng, Nature 515 (2014) 96–99.
- [21] O.F. Aldosari, S. Iqbal, P.J. Miedziak, G.L. Brett, D.R. Jones, X. Liu, J.K. Edwards, D.J. Morgan, D.K. Knight, G.J. Hutchings, Catal. Sci. Technol. 6 (2016) 234–242.
- [22] P. Verma, Y. Kuwahara, K. Mori, H. Yamashita, J. Mater. Chem. A 4 (2016) 10142–10150.
- [23] A. Kim, C. Sanchez, G. Patriarche, O. Ersen, S. Moldovan, A. Wisnet, C. Sassoie, D.P. Debecker, Catal. Sci. Technol. 6 (2016) 8117–8128.
- [24] H. Kominami, A. Furusho, S.-Y. Murakami, H. Inoue, Y. Kera, B. Ohtani, Catal. Lett. 76 (2001) 31–34.
- [25] H. Zhu, Q. Wang, L. Cheng, R. Addou, J. Kim, M.J. Kim, R.M. Wallace, ACS Nano 11 (11) (2017) 11005–11014.
- [26] C. Newman, X. Zhou, B. Goundie, I.T. Ghampson, R.A. Pollock, Z. Ross, M.C. Wheeler, R.W. Meulenber, R.N. Austin, B.G. Frederick, Appl. Catal. A Gen. 477 (2014) 64–74.
- [27] C. Hernandez-Mejia, E.S. Gnanakumar, A. Olivos-Suarez, J. Gascon, H.F. Greer, W. Zhou, G. Rothenberg, N. Raveendran Shiju, Catal. Sci. Technol. 6 (2016) 577–582.
- [28] P.D. Vaidya, V.V. Mahajani, Appl. Catal. B Environ. 51 (2004) 21–31.
- [29] J.A. Baeza, L. Calvo, J.J. Rodriguez, E. Carbó-Argibay, J. Rivas, M.A. Gilarranz, Appl. Catal. B Environ. 168–169 (2015) 283–292.
- [30] Y. Jiao, A. Hellman, Y. Fang, S. Gao, M. Kall, Sci. Rep. 5 (2015) 11374.
- [31] S. Picozzi, A. Pecchia, M. Gheorghe, A. Di Carlo, P. Lugli, B. Delley, M. Elstner, Phys. Rev. B 68 (2003).
- [32] S. Rajput, M.X. Chen, Y. Liu, Y.Y. Li, M. Weinert, L. Li, Nat. Commun. 4 (2013) 2752.
- [33] C. Gong, L. Colombo, R.M. Wallace, K. Cho, Nano Lett. 14 (2014) 1714–1720.
- [34] W. Dang, H. Chen, N. Umezawa, J. Zhang, Phys. Chem. Chem. Phys. 00 (2015) 1–9.
- [35] J. Zhang, W. Dang, X. Yan, M. Li, H. Gao, Z. Ao, Phys. Chem. Chem. Phys. 16 (2014) 23476–23482.
- [36] J. Zhang, W. Dang, Z. Ao, S.K. Cushing, N. Wu, Phys. Chem. Chem. Phys. 17 (2015) 8994–9000.
- [37] W. Siripala, A. Ivanovskaya, T.F. Jaramillo, S.-H. Baeck, E.W. McFarland, Sol. Energy Mat. Sol. C 77 (2003) 229–237.
- [38] M.C. Ortega-Liebana, J.L. Hueso, S. Ferdousi, R. Arenal, S. Irusta, K.L. Yeung, J. Santamaria, Appl. Catal. B Environ. 218 (2017) 68–79.
- [39] S.-T. Zhang, C.-M. Li, H. Yan, M. Wei, D.G. Evans, X. Duan, J. Phys. Chem. C 118 (2014) 3514–3522.
- [40] J. Zhang, M. Zhang, Y. Han, W. Li, X. Meng, B. Zong, J. Phys. Chem. C 112 (2008) 19506–19515.
- [41] T.O. Omotoso, B. Baek, L.C. Grabow, S.P. Crossley, ChemCatChem 9 (14) (2017) 2642–2651.
- [42] Y. Hou, X.-Y. Li, Q.-D. Zhao, X. Quan, G.-H. Chen, Adv. Funct. Mater. 20 (2010) 2165–2174.
- [43] A.R. Puigdollers, P. Schlexer, G. Pacchioni, J. Phys. Chem. C 119 (2015) 15381–15389.
- [44] Y. Zou, X. Wang, A. Khan, P. Wang, Y. Liu, A. Alsaedi, T. Hayat, X. Wang, Environ. Sci. Technol. 50 (2016) 7290–7304.
- [45] Y. Kakuma, A.Y. Nosaka, Y. Nosaka, Phys. Chem. Chem. Phys. 17 (2015) 18691–18698.
- [46] G.M. King, Sarwat Iqbal, P.J. Miedziak, G.L. Brett, Simon A. Kondrat, B.R. Yeo, X. Liu, J.K. Edwards, D.J. Morgan, D.K. Knight, G.J. Hutchings, ChemCatChem 7 (2015) 2122–2129.
- [47] J. Sun, X. Li, Q. Zhao, M.O. Tadé, S. Liu, Appl. Catal. B Environ. 219 (2017) 259–268.
- [48] F. Zhang, X. Li, Q. Zhao, D. Zhang, ACS Sustain. Chem. Eng. 4 (2016) 4554–4562.
- [49] L. Zhang, Y. Li, Q. Zhang, H. Wang, CrystEngComm 15 (2013) 5986.
- [50] F.X. Xiao, S.F. Hung, J. Miao, H.Y. Wang, H. Yang, B. Liu, Small 11 (2015) 554–567.
- [51] X. Li, S. Fang, L. Ge, C. Han, P. Qiu, W. Liu, Appl. Catal. B Environ. 176–177 (2015) 62–69.
- [52] C. Han, L. Wu, L. Ge, Y. Li, Z. Zhao, Carbon 92 (2015) 31–40.
- [53] B.Y. Chang, S.M. Park, Annu. Rev. Anal. Chem. 3 (2010) 207–229.
- [54] Y. Yalçın, M. Kılıç, Z. Çınar, Appl. Catal. B Environ. 99 (2010) 469–477.
- [55] X. Yu, T. Hou, X. Sun, Y. Li, ChemPhysChem 13 (2012) 1514–1521.
- [56] M.R. Khan, T.W. Chuan, A. Yousuf, M.N.K. Chowdhury, C.K. Cheng, Catal. Sci. Technol. 5 (2015) 2522–2531.
- [57] A.M. Lacerda, University of London, University of London, 2015.
- [58] A.L. Linsebigler, G. Lu, J.T. Yates, Chem. Rev. 95 (1995) 735–758.
- [59] H.B. Michaelson, J. Appl. Phys. 48 (1977) 4729–4733.
- [60] Z. Jiang, W. Wan, W. Wei, K. Chen, H. Li, P.K. Wong, J. Xie, Appl. Catal. B Environ. 204 (2017) 283–295.
- [61] A. Khanna, V.K. Shetty, Sol. Energy 99 (2014) 67–76.
- [62] X. Zhao, T. Xu, W. Yao, C. Zhang, Y. Zhu, Appl. Catal. B Environ. 72 (2007) 92–97.
- [63] J. Döfling, B.K. Harrison, Environ. Sci. Technol. 2 (1992) 2213–2218.
- [64] D. Chen, A.K. Ray, Chem. Eng. Sci. 56 (2001) 1561–1570.